RESEARCH ARTICLE
ATMOSPHERIC PHYSICS

Earth and Planetary Physics
10: 259–268, 2026
doi: 10.26464/epp2026032

High-latitude mesospheric water vapor trends evaluated with a new method from SABER data

Xi Kang[1,2], ChengYun Yang[1,2*], and Tao Li[1,2]

[1]National Key Laboratory of Deep Space Exploration/School of Earth and Space Sciences, University of Science and Technology of China, Hefei 230026, China;
[2]Chinese Academy of Sciences (CAS) Center for Excellence in Comparative Planetology/CAS Key Laboratory of Geospace Environment/Mengcheng National Geophysical Observatory, University of Science and Technology of China, Hefei 230026, China

Key Points:

- A new local-time binning (LT-mode) method corrects orbital drift and reduces tidal aliasing in Sounding of the Atmosphere using Broadband Emission Radiometry (SABER)/Thermosphere–Ionosphere–Mesosphere Energetics and Dynamics (TIMED) high-latitude trend analysis.
- Simulation experiments demonstrate that the LT-mode method effectively handles high-latitude SABER data without relying on empirical models.
- The LT-mode analysis shows strong drying over northern high latitudes in winter and summer, whereas southern high-latitude trends are weak or insignificant.

Citation: Kang, X., Yang, C. Y., and Li, T. (2026). High-latitude mesospheric water vapor trends evaluated with a new method from SABER data. *Earth Planet. Phys.*, *10*(2), 259–268. http://doi.org/10.26464/epp2026032

Abstract: In this study, we use observations from the Sounding of the Atmosphere using Broadband Emission Radiometry (SABER) instrument onboard the Thermosphere–Ionosphere–Mesosphere Energetics and Dynamics (TIMED) satellite to develop and apply a new local-time binning method to investigate the long-term evolution of mesospheric water vapor at high latitudes. The proposed method accounts for the gradual local-time drift of the SABER orbit by aligning seasonal observation windows and selecting samples observed at similar local times. This approach minimizes tidal aliasing and ensures more consistent sampling, yielding more reliable estimates of long-term water vapor trends at high latitudes. The results show that drying signals primarily appear in the polar regions. However, in the southern hemisphere, a drying trend is observed only in autumn, whereas winter and summer mainly show moistening trends. In contrast, the northern hemisphere exhibits drying signals in the polar regions during all seasons, showing a clear seasonal asymmetry. Additionally, the water vapor trend in the northern hemisphere is particularly pronounced in February (late winter), with moistening reaching up to +2.0 ppmv. The winter in the southern hemisphere (July–August) also shows moistening, but the trend is still weaker than in the northern hemisphere. These differences highlight the strong moistening trend in the northern hemisphere during winter and underscore the significant asymmetry in seasonal water vapor changes between the two hemispheres. These findings emphasize the limitations of water vapor trend estimates across different seasons and latitudes. Moreover, they provide new insights into the spatiotemporal variability associated with tidal structures, underscoring the importance of optimizing local-time sampling strategies for reliable long-term trend detection.

Keywords: mesospheric water vapor; high-latitude region; SABER/TIMED observations; long-term trend; local-time sampling bias

1. Introduction

The stratosphere and mesosphere form a key transition region between Earth's weather and space weather, characterized by strong dynamical–chemical coupling (Khosrawi et al., 2018; Gu SY et al., 2024, 2025; Sheng Z et al., 2025). Over the past two decades, multi-source observations and model simulations have consistently revealed a gradual global-scale increase in stratospheric–mesospheric water vapor (H_2O; Hegglin et al., 2014; Yue J et al., 2019; Konopka et al., 2022; Sheese et al., 2025). However, the magnitude and vertical structure of this trend exhibit pronounced height and latitude dependencies, and large discrepancies remain among different datasets in the upper atmosphere (above ~0.2 hPa; Shi GC et al., 2023). Long-term records from balloon-borne frost point hygrometers, ground-based microwave radiometers, and merged satellite products suggest a slow increase of ~0.1–0.3 ppmv decade^{-1} in the low- to midlatitude mesosphere since the late 20th century (Randel et al., 2006; Hurst et al., 2011; Dessler et al., 2014; Yu WD et al., 2022; Nedoluha et al., 2023; Zhang SR et al., 2023). Observations from the Halogen Occultation Experiment (HALOE), Atmospheric Chemistry Experi-

First author: X. Kang, kx_0045@mail.ustc.edu.cn
Correspondence to: C. Y. Yang, cyyang@ustc.edu.cn
Received 02 NOV 2025; Accepted 22 JAN 2026.
First Published online 12 FEB 2026.

ment–Fourier Transform Spectrometer (ACE-FTS), and Stratospheric Aerosol and Gas Experiment (SAGE) generally indicate positive water vapor trends between 20 and 60 km (Froidevaux et al., 2015), whereas the Microwave Limb Sounder (MLS) and the Sounding of the Atmosphere using Broadband Emission Radiometry (SABER) suggest smaller increases of approximately 0.1–0.3 ppmv decade^{-1} (Yue J et al., 2019). The SABER retrievals above approximately 60–80 km are significantly affected by nonlocal thermodynamic equilibrium effects, background temperature uncertainties, and retrieval assumptions, which lead to substantial discrepancies in long-term trend estimates and seasonal amplitudes (Remsberg et al., 2018; Rong PP et al., 2019; Shi GC et al., 2023). Model studies indicate that the tropical tropopause temperature, Brewer–Dobson circulation strength, and methane (CH_4) oxidation jointly drive the interdecadal evolution of water vapor (Yu WD et al., 2022). Building on these studies, Whole-Atmosphere Community Climate Model (WACCM) simulations show that mesospheric water vapor trends arise partly from methane dissociation above ~65 km and partly from vertical transport of lower-level water vapor (Yu WD et al., 2023b), whereas recent SD-WACCM6 (Specified Dynamics Whole Atmosphere Community Climate Model version 6) results confirm the dominant role of methane in long-term changes at high latitudes (Sheese et al., 2025).

Previous multi-dataset analyses have shown that mesospheric water vapor at low to midlatitudes generally exhibits a positive long-term trend of approximately 0.1 ppmv decade^{-1}, with an increase in magnitude toward higher altitudes (Yu WD et al., 2022; Zhang SR et al., 2023). Compared with long-term assessments of water vapor at low latitudes, assessments at high latitudes remain limited because of sparse ground-based observations and the scarcity of continuous satellite records, despite the fact that polar middle-atmospheric dynamics play a key role in interhemispheric coupling and large-scale circulation variability (Yang CY et al., 2022). Recent efforts combining ground-based microwave radiometers with Aura-MLS and reanalysis data have improved understanding of polar variability (e.g., Shi GC et al., 2023), yet significant uncertainties persist in long-term trend evaluations, particularly for SABER. The yaw-cycle (YC) method (Liu X et al., 2024) has been successfully applied to correct SABER polar temperatures. However, because it relies on the MSIS2.0 (Mass Spectrometer and Incoherent Scatter radar, version 2.0) temperature field to remove seasonal variations, the method cannot be directly used for water vapor analysis. Consequently, robust evaluation of long-term trends in high-latitude mesospheric water vapor remains highly challenging.

To address these issues, we aim to improve the assessment of long-term high-latitude water vapor variability by accounting for the sampling limitations of SABER observations. This work seeks to mitigate the effects of orbital local-time (LT) drift and incomplete temporal coverage by providing a more consistent basis for evaluating the interdecadal evolution of polar mesospheric water vapor. The remainder of this article is organized as follows. Section 2 describes the datasets and analysis procedures. Section 3 presents the results of water vapor trend analyses in the mesosphere–lower thermosphere, and Section 4 discusses the reliability and implications of these trends and summarizes the main findings.

2. Data and Methods

2.1 SABER Datasets

The Thermosphere–Ionosphere–Mesosphere Energetics and Dynamics (TIMED) satellite was launched by the National Aeronautics and Space Administration (NASA) on December 7, 2001, to study the energy balance and dynamical processes from the mesosphere to the thermosphere. Its primary payload, the SABER, is designed to measure temperature, energy transport, and radiative characteristics in the middle and upper atmosphere (Russell et al., 1999). The TIMED satellite operates in a near-polar orbit (non-sun-synchronous) at an altitude of approximately 625 km, with an orbital period of ~97 min, and achieves nearly 22 h of LT coverage over a 60-d cycle.

The SABER instrument utilizes broadband infrared radiometry combined with limb-scanning geometry to retrieve profiles of temperature, density, and chemical species from infrared emissions of CO_2, O_3, and H_2O. Its spectral coverage spans 1.6–17 μm with a vertical resolution of ~2 km. Since 2002, SABER has provided temperature profiles covering 53°S–83°N (northward viewing) and 83°S–53°N (southward viewing) over an altitude range of ~15–110 km. The H_2O volume mixing ratio product (version 2.07) extends from ~100 hPa (~16 km) to ~0.006 hPa (~83 km), also with a vertical resolution of ~2 km. Compared with the solar occultation sampling of the HALOE, SABER radiance measurements provide a significantly larger data volume and more uniform coverage in the upper atmosphere.

The SABER instrument operates in alternating YCs, observing one hemisphere at a time. During northward-viewing periods, SABER measures from approximately 55°S to 85°N, whereas during southward-viewing periods it covers 55°N to 85°S. Each YC typically lasts approximately 60 d, meaning that the two high-latitude regions (55°–85°N and 55°–85°S) are not observed simultaneously and that observations at a given latitude are temporally discontinuous.

2.2 Data Processing Method

Compared with the absolute magnitude of mean temperature, the amplitude of long-term trends is relatively small and thus requires extra caution in determination. Figure 1 compares the LT sampling between high and low latitudes on a given day, where it can be seen that at high latitudes, the LT coverage is more concentrated because of orbital geometry constraints, leading to uneven spatiotemporal sampling in certain regions.

Figure 2 illustrates the temporal distribution of SABER sampling and is used to identify latitude–altitude bands with high data coverage for trend analysis. As illustrated in Figure 2, the temporal distribution of SABER observations in the northern hemisphere from 2002 to 2021 indicates that the observation period has gradually shifted earlier by more than one month. Because SABER alternates its high-latitude observations between the northern and southern hemispheres, each lasting approximately 60 d, the coverage in each hemisphere is discontinuous and occurs roughly

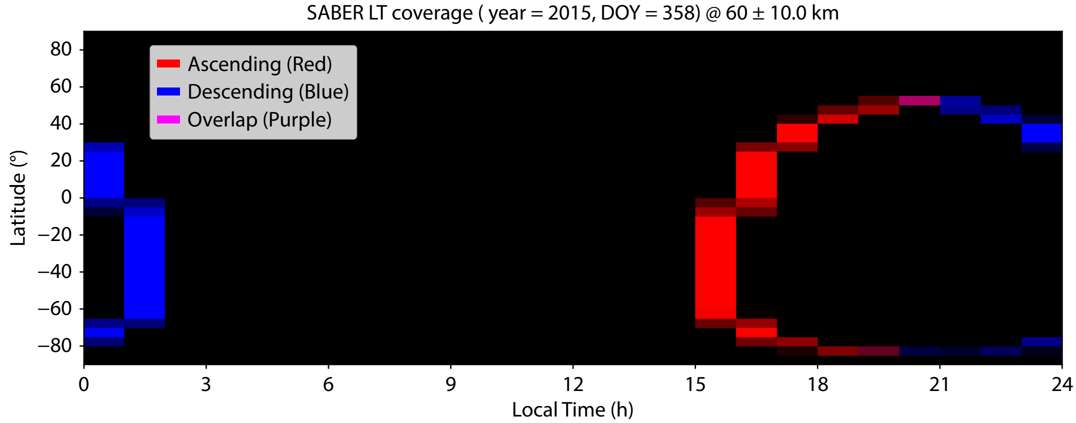

Figure 1. Local-time coverage of SABER observations on December 24, 2015 for different latitude bands. Red shading indicates ascending orbits, blue shading indicates descending orbits, and purple shading indicates overlapping orbits.

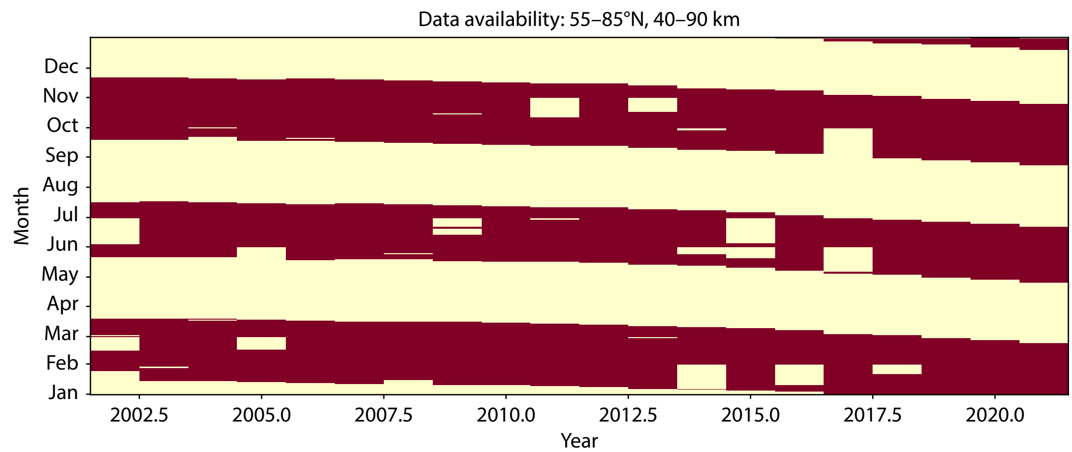

Figure 2. Daily observation availability of SABER measurements from 2002 to 2021 in the 55–85°N, 40–90 km region. Red shading indicates days with valid observations, and light yellow shading denotes days without data.

3 times per year. Because the timing of these observation windows gradually shifts from year to year, using all available data directly in a trend analysis could mix seasonal variability with long-term changes. To mitigate this aliasing effect, the analysis focuses on the period 2002–2021, and data selection is guided by the spatiotemporal distribution of valid SABER observations. Specifically, a day is considered valid if measurements exist for at least 90% of the years. Adjacent valid days must be separated by no more than 5 d, and each continuous sequence of valid days must last at least 10 d. A band is thus defined as a temporally continuous observational segment within the specified latitude–altitude domain—namely 55°–80° in each hemisphere and 40–80 km in altitude—that satisfies these criteria. On the basis of this procedure, three observationally stable time bands are identified in the northern hemisphere—February 1–22 (22 d), June 1–13 (13 d), and September 19–October 25 (37 d)—and three corresponding bands are identified in the southern hemisphere—March 19–April 30 (43 d), July 16–August 24 (39 d), and November 21–December 20 (29 d). These stable periods provide consistent temporal sampling across most years, offering a reliable basis for multi-year averaging and long-term trend estimation.

To reduce the interference of atmospheric wave activity (including gravity waves, tides, and planetary waves) on the long-term trend analysis, we first remove their short-term variability to obtain more stable background fields. In particular, the use of zonal mean values effectively suppresses the influence of small-scale gravity waves, nonmigrating tides, and long-period planetary waves, thereby allowing a more accurate estimation of mean water vapor trends. However, migrating tides depend on LT and exhibit strong amplitudes in the upper atmosphere, making them impossible to remove simply through zonal averaging. To obtain reliable long-term trends, it is therefore necessary to first fit and remove the influence of atmospheric diurnal tides. Given that tidal signals also show interannual variability, this study establishes a systematic tidal-fitting procedure for SABER temperature observations to quantitatively characterize the spatial and temporal structures of the semidiurnal (12-h) and diurnal (24-h) tidal components in the middle and upper atmosphere. To lessen the impact of local anomalous samples, a moving time-window strategy is applied (Figure 3), in which observational data from 2002 to 2021 are processed using a 5-year sliding window to ensure adequate data coverage within each fitting period. For each window, valid observations within the target latitude range (−55°–90°) and altitude range (40–90 km) are selected and averaged by LT with a bin size of 0.5 h to construct representative

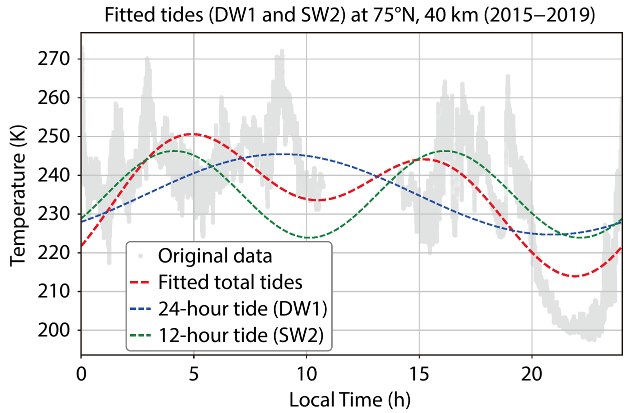

Figure 3. Example of the tidal fitting process at 75°N and 40 km within a 5-year window. The gray dots represent daily water vapor values at different local times, whereas the red line indicates the fitted tidal curve. The blue and green lines denote the individual DW1 and SW2 tidal components, respectively.

diurnal tidal variation curves.

On the basis of the processed LT temperature fields, a two-component harmonic analysis is performed at each latitude–altitude grid point to resolve the diurnal (24-h) and semidiurnal (12-h) migrating tidal components. The fitting provides the amplitudes and unwrapped phases (in LT) of both tidal modes, which are used to reconstruct and remove the tidal contributions from the original temperature data. This step ensures that variations associated with changing LT sampling across different years do not alias into the long-term trend analysis. Because tidal phases exhibit temporal variability, a two-step fitting procedure is utilized to ensure consistency across different locations and time periods. In the first step, the median phase of each migrating tidal component is determined from the initial harmonic analysis and fixed as a reference. In the second step, the fitting is repeated with the phase held constant, allowing only the amplitude to vary. This approach provides a uniform phase baseline, enabling robust cross-comparisons of tidal amplitudes among different latitude–altitude grid points and preventing phase drift from introducing artificial variability. The entire procedure is implemented using a nonlinear least-squares optimization algorithm and includes an automatic quality-control criterion that excludes time windows with insufficient data, thereby ensuring the statistical robustness of the retrieved tidal parameters:

$$H_2O_{res} = H_2O_{bk} + \sum_{n=1}^{2} a_n \cos\left(n\,\omega\, t_{LT} - \phi_n\right).$$

Among them, $\omega = 2\pi/24$ represents the Earth's rotational frequency (radians per hour); t_{LT} denotes the LT (hours); and a_n and ϕ_n are the amplitudes and phases of the migrating diurnal tide (n = 1) and semidiurnal tide (n = 2), respectively. In this way, H_2O_{bk} excludes atmospheric wave perturbations and can be regarded as the mean water vapor concentration.

When conducting long-term trend analyses with satellite observations, the variation in LT sampling can strongly influence the detected trends, as measurements at different LTs may reflect different phases of the diurnal cycle. To address this issue, we introduce an LT-mode approach, in which long-term variations are evaluated at fixed LTs to minimize sampling-induced biases. Figure 4 illustrates the LT coverage for the February observation window in the northern hemisphere, comparing data from 2002 and 2021. Even within the same seasonal period, the LT coverage gradually drifts from year to year because of orbital precession, resulting in substantial cumulative differences after two decades. This drift is further illustrated in Figure 5: prior to 2016, the LT sampling was approximately uniform, but after 2016—when the orbit entered a configuration lacking noontime observations—the LT distribution became markedly nonuniform. Under such conditions, directly removing tides using the full LT data would introduce diurnal aliasing into the derived long-term trends, thereby reducing their reliability.

To resolve this issue, we develop an LT-mode approach that standardizes the analysis at fixed LT intervals. Specifically, histograms of the 20-year record are used to identify the most frequently occurring LT intervals that persist across all years, which are defined as the LT modes. These modes are refined through bin-width interpolation to capture the precise centers of the dominant

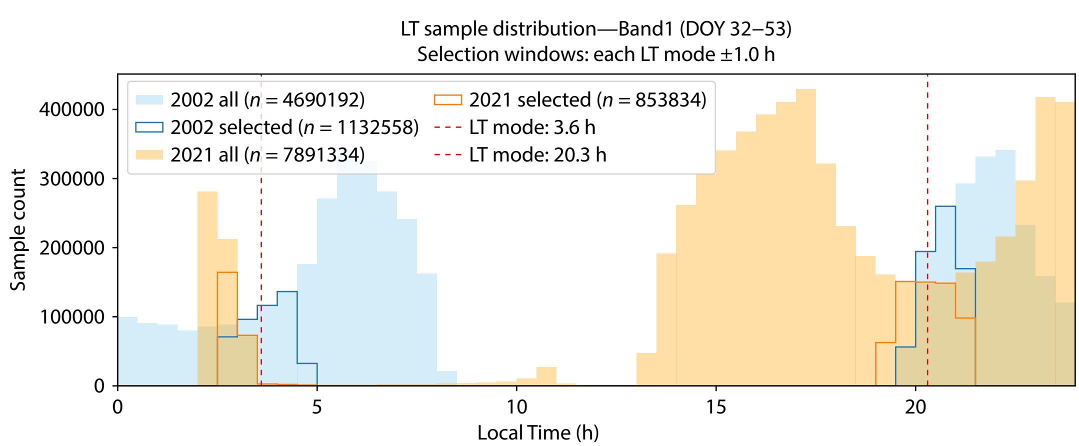

Figure 4. Local-time sampling distribution for the February observation window in the northern hemisphere. The *x*-axis represents LT, and the *y*-axis indicates the number of valid SABER observations. The blue and yellow bars correspond to data from 2002 and 2021, respectively. The red dashed line marks the selected central LT, and the boxed region denotes the subset of data used in the analysis.

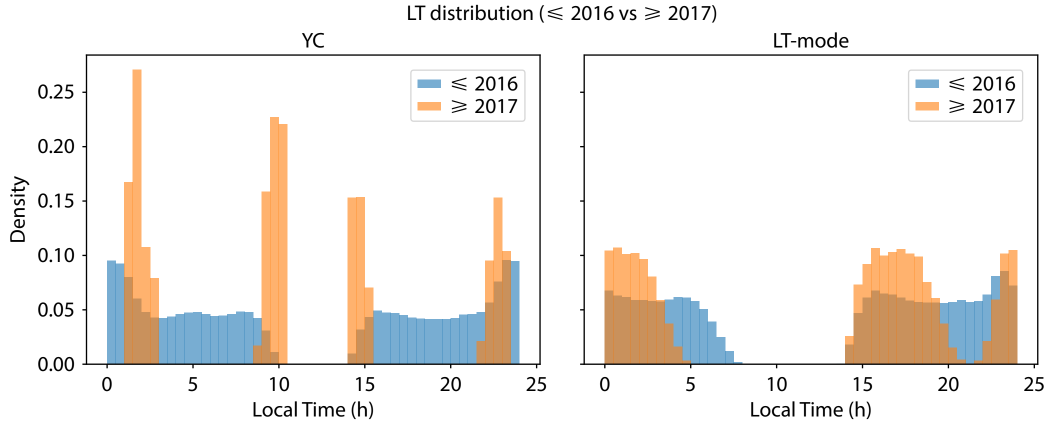

Figure 5. Sampling comparison across the LT discontinuity: YC method versus LT-mode.

LT coverage. Two fixed LT-mode windows are then established, and a tolerance of ±1 h around each mode is applied to ensure sufficient sampling while maintaining temporal comparability between early and late years. It should be noted that during the tidal-fitting stage, the full LT data are still utilized to preserve the complete diurnal structure, whereas the LT-mode subsets are used in the subsequent long-term trend analysis.

Whereas the LT-mode approach effectively standardizes LT sampling, its necessity arises from the fact that tidal removal alone cannot completely eliminate diurnal contamination. In an ideal situation, if the fitted tides were perfectly removed, the true daily mean values could be directly recovered. In practice, however, tidal amplitudes and phases vary with time, and the 5-year sliding window used in the fitting cannot fully capture these variations, leaving nonlinear residual anomalies. To quantitatively assess how much the LT-mode constraint improves the long-term trend estimation, we designed a variable-tide experiment.

In this experiment, a synthetic temperature record was generated with time-varying tidal amplitudes and phases, and random noise was added to simulate a 20-year observational period. Two methods were compared:

(1) *All-LT method*: Tides are fitted using all LT samples within each 5-year window, and the residuals are averaged over a ±30-d monthly window to obtain the monthly mean.

(2) *LT-mode method*: This method applies the same 5-year tidal fitting but retains only samples within fixed LT windows (two global modes ±3 h) when computing the residual mean, thereby reducing aliasing errors attributable to LT sampling drift.

As shown in Figure 6 and Table 1, both methods reproduce the imposed long-term trend reasonably well (mean error within 0.5 K decade^{-1}). However, the All-LT method is subject to stronger aliasing under time-varying tides, leading to larger biases. In contrast, the LT-mode method effectively suppresses aliasing and yields trend estimates closer to the true value. Although its error variance is slightly higher, its overall robustness is improved. These results demonstrate that the LT-mode method provides a more reliable framework for extracting long-term trends from satellite observations.

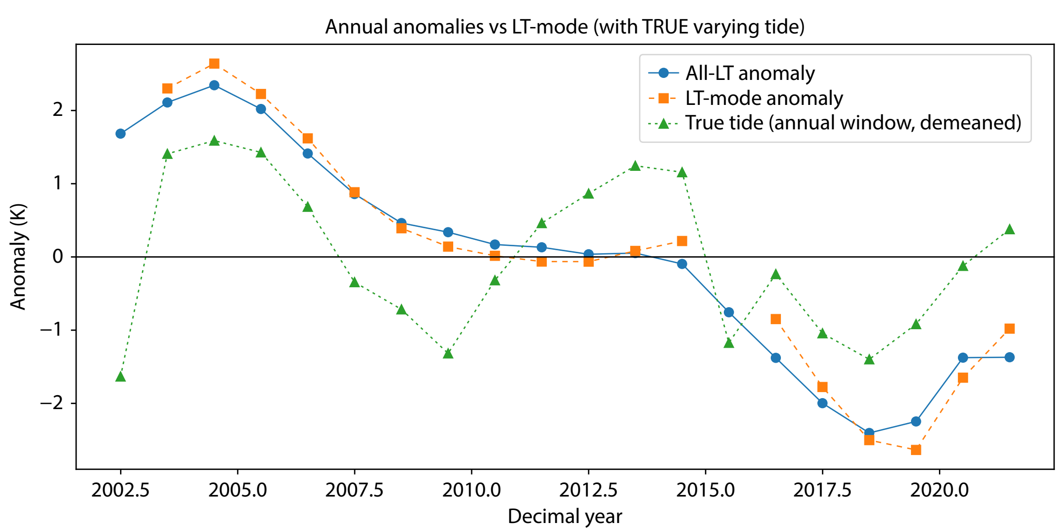

Figure 6. Comparison of long-term trend estimates obtained using the All-LT and LT-mode methods in the variable-tide experiment. The true imposed trend is $\beta = -2.5$ K decade^{-1}. The green dashed line with triangles represents the prescribed time-varying tidal amplitudes used in the simulation. The blue circles indicate the results derived from the All-LT method, and the orange dashed lines with square symbols denote those obtained using the LT-mode method.

Table 1. Trend ± SE across five seeds for each method.

Method	seed1	seed2	seed3	seed4	seed5
All-LT (5-year tide, annual 60 d)	−2.35 ± 0.19	−2.35 ± 0.19	−2.34 ± 0.19	−2.34 ± 0.19	−2.34 ± 0.19
LT-mode (5-year tide, annual 60 d)	−2.51 ± 0.26	−2.51 ± 0.27	−2.50 ± 0.27	−2.50 ± 0.27	−2.50 ± 0.27

After confirming the reliability of the LT-mode method in the variable-tide experiment, we applied it to the SABER temperature dataset to estimate mesospheric long-term trends. To further validate the applicability of the LT-mode trend-retrieval framework to real observations, we performed an independent comparison using SABER temperature data. Following the same analysis procedure, long-term mesospheric temperature trends were derived for the southern hemisphere November–December period and compared with the results of Liu X et al. (2024), who analyzed SABER data without applying LT-mode constraints. As shown in Figure 7, the LT-mode results exhibit spatial patterns and magnitudes that are highly consistent with Liu's YC6 case (their Figure 4), with only minor regional differences near 60°–70°S, demonstrating the consistency of long-term trend retrievals between the two approaches. This agreement demonstrates that the LT-mode approach produces reliable trend estimates and does not introduce systematic biases, confirming the robustness of the method when applied to satellite observations.

To accurately estimate the long-term trends of mesospheric water vapor, interannual variability associated with natural climate drivers should be accounted for. The 10.7 cm solar radio flux ($F_{10.7}$) is adopted as an independent variable in the regression model, given its established utility in characterizing solar cycle variations in the middle atmosphere (Tapping et al., 2013; Forbes et al., 2014). In addition to solar activity, the El Niño–Southern Oscillation (ENSO) is also included as a regressor to account for its significant teleconnection impacts on the stratosphere and their subsequent dynamical coupling to higher altitudes (Domeisen et al., 2019). ENSO—although originating in the tropical ocean–atmosphere system—has been shown to influence the middle and upper atmosphere at middle and high latitudes through large-scale dynamical coupling (e.g., Li T et al., 2013, 2016; Cen YT et al., 2022). Therefore, ENSO is included in the multiple linear regression to avoid aliasing its variability into the estimated long-term trend.

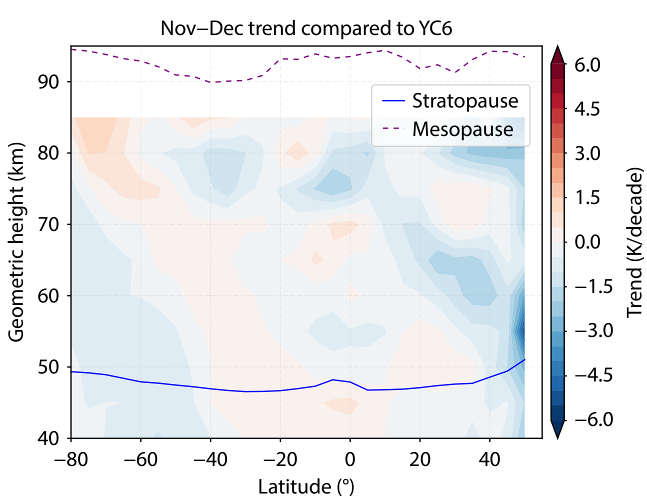

Figure 7. Southern hemisphere (November–December) mesospheric temperature trends derived using the LT-mode method, compared with the YC6 results reported by Liu et al. (2024, their Figure 4).

The regression equation is expressed as

$$Y(t) = c_0 + c_1 t + c_2 F_{10.7}(t) + c_3 \mathrm{ENSO}(t) + c_4 AP(t) + \varepsilon(t),$$

where Y denotes the annual mean water vapor concentration from 2002 to 2023; c_0 represents the mean state; c_1 indicates the long-term trend; and c_2 and c_3 represent the contributions from solar activity and ENSO, respectively. Here, AP represents a geomagnetic activity index to account for the impact of particle precipitation and auroral activity on mesospheric chemistry, while $\varepsilon(t)$ is the residual term encompassing both model uncertainty and random observational noise. The regression was performed for the period 2002–2021; data after 2021 were excluded to avoid potential biases caused by the Hunga Tonga–Hunga Ha'apai eruption in early 2022, which temporarily disturbed global mesospheric temperatures (Yu WD et al., 2023a) and injected massive amounts of water vapor and aerosols whose complex stratospheric transport and residence time could further confound long-term trend analysis (Zhao Q and Zhou X, 2026).

3. Results

Having validated the LT-mode framework by using both numerical experiments and independent comparisons with previous studies, we next applied this method to the SABER water vapor observations to investigate the long-term variability in the mesosphere.

Figure 8 shows the climatological distribution of mesospheric water vapor over the polar regions (40–85 km), for better understanding of the background state against which the long-term trends are interpreted. Figures 8a–8c present seasonal distributions of the water vapor mixing ratio in the northern hemisphere, whereas Figures 8d–8f show the corresponding distribution in the southern hemisphere. In boreal late winter (February; Figure 8a), water vapor mixing ratios are generally <2 ppmv above ~70 km, whereas values below ~60 km can reach ~8–10 ppmv. During boreal early summer (June; Figure 8b), the altitude where H_2O exceeds ~5 ppmv rises to ~75–80 km. In boreal autumn (September to October; Figure 8c), enhanced water vapor is primarily confined below ~60 km, with a maximum of ~10 ppmv, whereas the upper mesosphere remains comparatively dry.

The southern hemisphere (Figures 8d–8f) exhibits seasonal behavior similar to that in the northern hemisphere, with enhanced water vapor in the high-latitude mesosphere during summer and a reduced water vapor mixing ratio during winter. This seasonal contrast reflects the combined effects of large-scale circulation and temperature-dependent saturation. Figure 8 therefore documents the climatological background state of mesospheric water vapor (e.g., Garcia, 1989; Smith, 2012).

Figure 9 shows the zonal-mean water vapor trend profiles for six

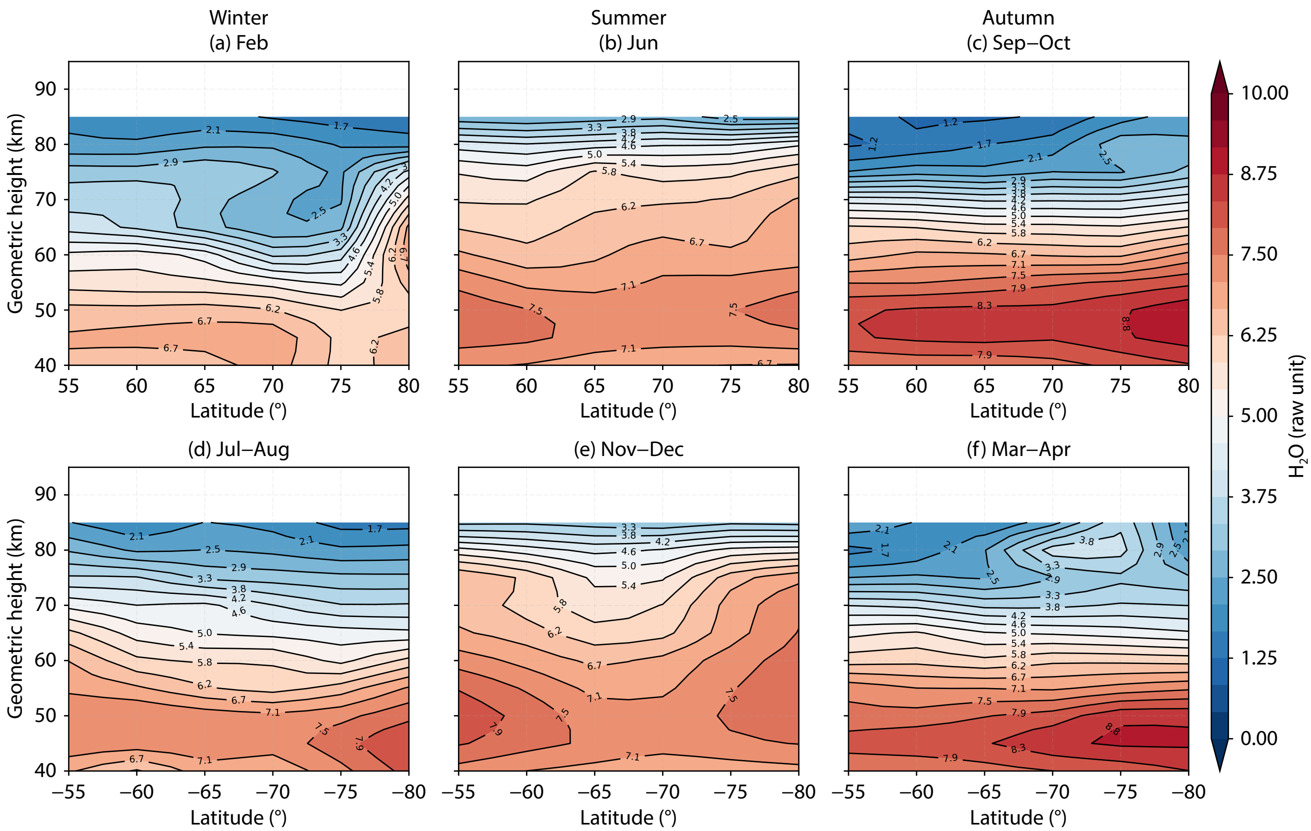

Figure 8. Water vapor distribution for the three northern hemisphere observation windows, corresponding to (a) February, (b) June, and (c) September–October, and southern hemisphere observation windows, corresponding to (d) July–August, (e) November–December, and (f) March–April. Contour labels indicate the trend values (ppmv decade^{-1}).

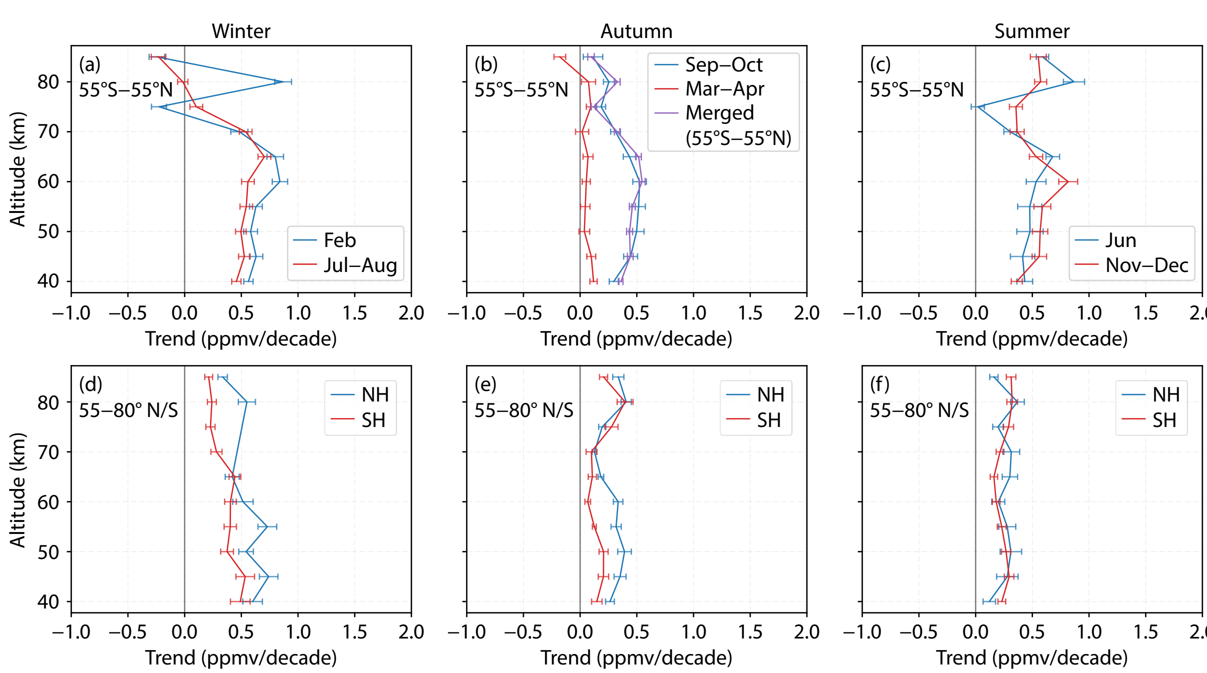

Figure 9. Corrected mean water vapor trends for the six observation bands. The trends are averaged over two latitude ranges: 55°S–55°N (global mean, red and blue lines in panels (a), (b), (c)) and 55–80°S or 55–80°N (polar regions, red and blue lines, respectively). Error bars indicate the standard errors of the averaged data. The overall mean trend (purple line) represents the mean of the six latitude-band trends within 55°S–55°N.

latitude bands, each corresponding to a specific period and the three seasonal observation windows in each hemisphere. The low-latitude trend profiles (Figures 9a–9c) show pronounced seasonal variability in their vertical structure. In the winter observation window (Figure 9a; February in the northern hemisphere and July–August in the southern hemisphere), trends differ above ~70 km. In the southern hemisphere, positive trends weaken above ~70 km and turn negative above ~80 km. In the northern hemisphere, the trend remains strongly positive near ~80 km but exhibits localized negative layers around ~75 km and ~85 km. Overall, the wintertime low-latitude trends therefore cannot be described as a simple moist-below/dry-above reversal at 70 km.

Figure 9b corresponds to September–October in the northern hemisphere and March–April in the southern hemisphere. The trends show a distinct hemispheric contrast, with significant moistening in the northern hemisphere, whereas the trends in the southern hemisphere are generally weak and mostly insignificant. In summer and winter (June and November–December; Figure 9c), the moistening trend dominates both hemispheres throughout the middle and upper mesosphere, with similar trends in both hemispheres.

The purple line in Figure 9b represents the mean trend of the analyzed periods averaged over 55°S–55°N among different months or seasons. It shows that low-latitude water vapor increases gradually within 40–60 km, reaching a maximum near 60 km, followed by a slight weakening between 60 and 80 km. This vertical profile agrees well with previous multi-dataset analyses: long-term observations indicate that mesospheric water vapor at low to midlatitudes generally exhibits a positive trend of approximately 0.1 ppmv decade^{-1} and increases with altitude (Yu WD et al., 2022; Zhang SR et al., 2023). Although discrepancies among satellite datasets above ~0.2 hPa (≈60 km) introduce uncertainty in the upper-level estimates (Shi GC et al., 2023), the standard errors in Figure 9 confirm that the moistening trend in the 70–80 km layer remains statistically significant and consistent with earlier results.

In the high-latitude regions of Figure 9d–9f, the seasonal dependence becomes more pronounced. In winter, the moistening trend is stronger in the northern hemisphere, with a trend of approximately 0.7–0.5 ppmv decade^{-1} in the lower mesosphere (below ~70 km) and a reduction to 0.5–0.3 ppmv decade^{-1} in the upper mesosphere (above ~70 km). In autumn (Figure 9e), both hemispheres exhibit moistening that intensifies with altitude, with trends ranging from approximately 0.2–0.3 ppmv decade^{-1} in the lower mesosphere to 0.4–0.5 ppmv decade^{-1} in the upper mesosphere. However, the southern hemisphere shows slightly drier conditions in the lower mesosphere, with a weaker moistening trend at the bottom (~0.2–0.3 ppmv decade^{-1}), whereas the northern hemisphere maintains a more consistent moistening trend throughout the vertical profile. In summer, both hemispheres experience a strong moistening trend of approximately 0.3 ppmv decade^{-1}, which remains nearly constant with height throughout the middle and upper mesosphere.

Figure 10 shows the decadal trends of the water vapor mixing ratio as a function of latitude for the northern hemisphere seasonal observation windows (a: February; b: June; c: September–October) and their southern hemisphere counterparts (d: July–August; e: November–December; f: March–April), providing a latitude-resolved view of the baseline spatial structure prior to summarizing hemispheric differences. Both hemispheres exhibit broadly similar latitude-dependent patterns, with positive water vapor trends prevailing at middle latitudes (55°–70°) and weaker or negative trends toward the polar regions (75° and poleward). In the northern hemisphere, this latitudinal structure is robust across all seasonal windows, characterized by increasing water vapor south of approximately 70°N and a drying tendency poleward of this latitude. This midlatitude–polar contrast is most pronounced in February, with moistening reaching up to +2 ppmv decade^{-1} at lower and middle latitudes and drying of approximately −2 ppmv decade^{-1} over the polar cap, whereas similar but weaker contrasts are evident in June and September–October. In the southern hemisphere, water vapor trends are generally positive across the middle and high latitudes during winter (July–August) and summer (November–December), with drying confined to austral autumn (March–April) south of ~70°S. In contrast to the northern hemisphere, where a persistent polar drying feature extends up to ~75–80 km, no comparably persistent polar drying is observed in the south. Overall, although the large-scale spatial patterns are broadly similar between the two hemispheres, polar drying and wintertime moistening are weaker in amplitude and more seasonally confined in the southern hemisphere.

4. Summary

This study presents a methodological framework for evaluating long-term water vapor variability in the upper mesosphere by using two decades of observations from the SABER instrument onboard the TIMED satellite. A new LT-mode method was developed to minimize aliasing effects caused by the nonuniform LT sampling of satellite measurements. By identifying the most frequently observed LT intervals and constraining the analysis within these windows, the LT-mode approach effectively suppresses diurnal contamination and orbital drift biases. Compared with the conventional All-LT approach, the LT-mode method provides a physically consistent and practical strategy for extracting long-term signals without relying on an empirical background model, thereby reducing system bias. Application of this method reveals distinct hemispheric and seasonal patterns in mesospheric water vapor trends. Overall, water vapor trends between 55 and 80 km are predominantly positive in both hemispheres, with stronger moistening during local winter compared with summer and autumn. At high latitudes, the hemispheric behavior differs. In the northern hemisphere, water vapor trends become negative poleward of ~75°N, indicating persistent drying over the polar cap. In contrast, in the southern hemisphere, trends poleward of ~75°S are generally weak or not statistically significant, rather than showing systematic drying. These results highlight a robust altitude-dependent moistening in the mesosphere–lower thermosphere, accompanied by a clear hemispheric asymmetry in polar trend behavior.

Although the LT-mode approach provides a consistent framework

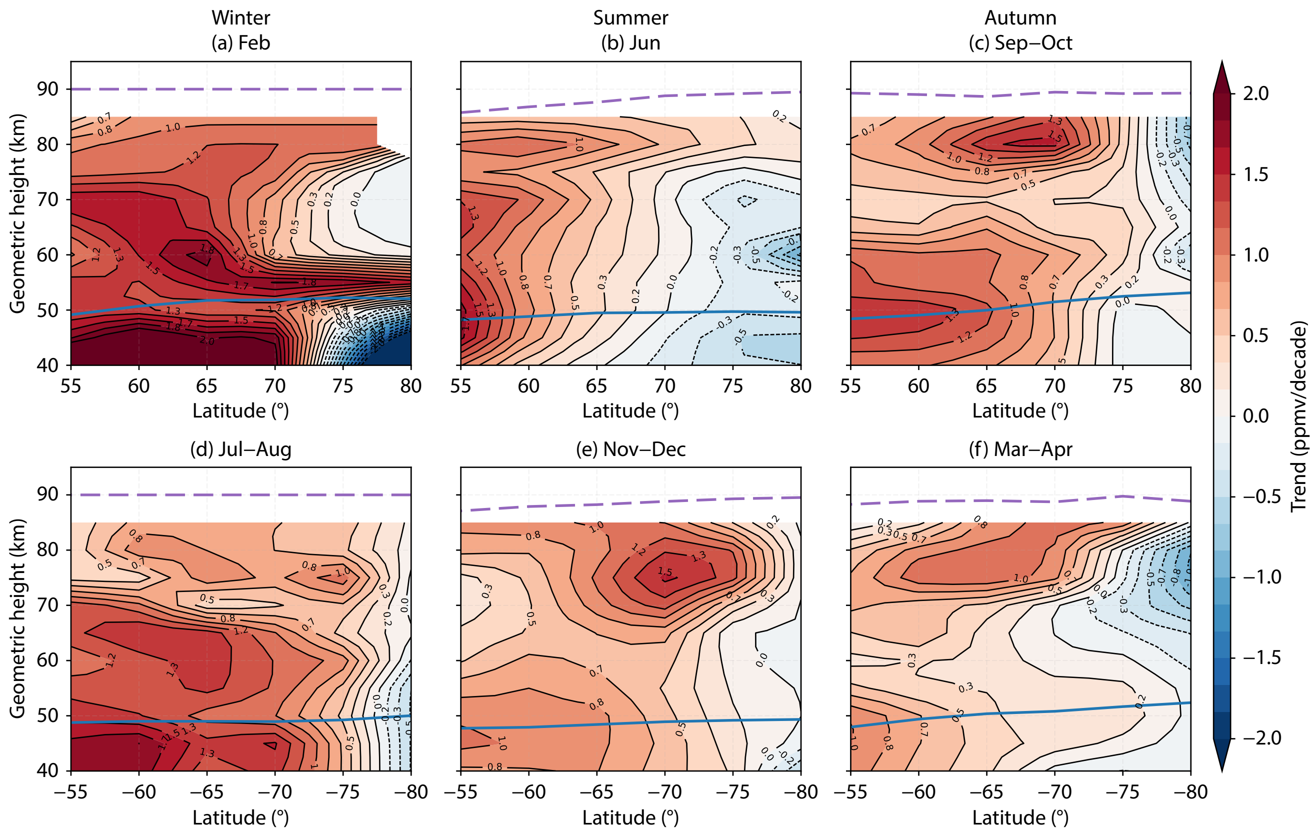

Figure 10. Mean water vapor trend distribution for the three northern hemisphere observation windows, corresponding to (a) February, (b) June, and (c) September–October, and southern hemisphere observation windows, corresponding to (d) July–August, (e) November–December, and (f) March–April. Contour labels indicate the trend values (ppmv decade^{-1}). The purple dashed line and blue solid line represent the climatological altitudes of the mesopause and stratopause, respectively. Blank areas denote grid points with fewer than 20 months of valid data, which are excluded from the analysis.

for evaluating such long-term changes, several uncertainties must still be considered. Measurement and retrieval errors increase with altitude, with random uncertainties reaching approximately 30% and systematic biases of 10%–20% in the upper mesosphere. Comparisons among satellite datasets generally show differences within ±10%, although SABER tends to overestimate water vapor near the Antarctic stratopause and underestimate it above 80 km in polar summer. Additional uncertainty arises from inter-sensor calibration inconsistencies above 0.2 hPa (~60 km) and from physical processes not fully captured by current models. Nevertheless, independent ground-based and multi-satellite records consistently indicate a long-term moistening, lending confidence to the general pattern observed here.

Mechanistic attribution of these trends remains complex. Decadal variability in the Brewer–Dobson circulation, tropical tropopause temperatures, methane oxidation, and solar forcing all contribute to mesospheric water vapor changes (Lossow et al., 2018; Yu WD et al., 2022). Continued observational and modeling efforts—particularly those combining chemistry–climate simulations with homogenized multi-satellite datasets—are essential to further constrain these mechanisms. The LT-mode framework developed in this study offers a transferable approach for isolating long-term atmospheric signals from nonuniform satellite sampling, providing a foundation for future analyses of trace gases and climate-related variability in the middle and upper atmosphere.

Acknowledgments

This work was supported by the National Key R&D Program of China (Grant No. 2022YFF0503703) and the National Natural Science Foundation of China (Grant Nos. 42130203, 42275133, and 42241135).

Data Availability

The SABER Level 2A data products (version 2.07) used in this study are publicly available from the NASA GATS/LaRC (Langley Research Center) data archive at https://saber.gats-inc.com/. The derived trend data and LT-mode fitting results can be obtained from the corresponding author upon reasonable request.

References

Cen, Y. T., Yang, C. Y., Li, T., Russell, J. M., III, and Dou, X. K. (2022). Suppressed migrating diurnal tides in the mesosphere and lower thermosphere region during El Niño in northern winter and its possible mechanism. *Atmos. Chem. Phys.*, *22*(12), 7861–7874. https://doi.org/10.5194/acp-22-7861-2022

Dessler, A. E., Schoeberl, M. R., Wang, T., Davis, S. M., Rosenlof, K. H., and Vernier, J. P. (2014). Variations of stratospheric water vapor over the past three decades. *J. Geophys. Res.: Atmos.*, *119*(22), 12588–12598. https://doi.org/10.1002/2014JD021712

Domeisen, D. I. V., Garfinkel, C. I., and Butler, A. H. (2019). The teleconnection of El Niño Southern Oscillation to the stratosphere. *Rev. Geophys.*, *57*(1), 5–47.

https://doi.org/10.1029/2018RG000596

Forbes, J. M., Zhang, X. L., and Marsh, D. R. (2014). Solar cycle dependence of middle atmosphere temperatures. *J. Geophys. Res.: Atmos.*, *119*(16), 9615–9625. https://doi.org/10.1002/2014JD021484

Froidevaux, L., Anderson, J., Wang, H. J., Fuller, R. A., Schwartz, M. J., Santee, M. L., Livesey, N. J., Pumphrey, H. C., Bernath, P. F., … McCormick, M. P. (2015). Global ozone chemistry and related trace gas data records for the stratosphere (GOZCARDS): Methodology and sample results with a focus on HCl, H_2O, and O_3. *Atmos. Chem. Phys.*, *15*(18), 10471–10507. https://doi.org/10.5194/acp-15-10471-2015

Garcia, R. R. (1989). Dynamics, radiation, and photochemistry in the mesosphere: Implications for the formation of noctilucent clouds. *J. Geophys. Res.: Atmos.*, *94*(D12), 14605–14615. https://doi.org/10.1029/JD094iD12p14605

Gu, S. Y., Wang, D., Qin, Y. S., Tang, L., Wei, Y. F., and Dou, X. K. (2024). Semiannual oscillation, annual oscillation, quasibiennial oscillation, and solar cycle variation of the OH airglow emission in the mesopause region. *Earth Planet. Phys.*, *8*(3), 479–496. https://doi.org/10.26464/epp2024026

Gu, S. Y., Zeng, Y. B., Hu, J., Qin, Y. S., Tang, L., and Liu, Y. X. (2025). Inter-hemispheric couplings in the middle atmosphere exhibited by principal component analysis of the SD-WACCM-X simulations. *Earth Planet. Phys.*, *9*(4), 925–937. https://doi.org/10.26464/epp2025046

Hegglin, M. I., Plummer, D. A., Shepherd, T. G., Scinocca, J. F., Anderson, J., Froidevaux, L., Funke, B., Hurst, D., Rozanov, A., … Weigel, K. (2014). Vertical structure of stratospheric water vapour trends derived from merged satellite data. *Nat. Geosci.*, *7*(10), 768–776. https://doi.org/10.1038/ngeo2236

Hurst, D. F., Oltmans, S. J., Vömel, H., Rosenlof, K. H., Davis, S. M., Ray, E. A., Hall, E. G., and Jordan, A. F. (2011). Stratospheric water vapor trends over Boulder, Colorado: Analysis of the 30 year Boulder record. *J. Geophys. Res.: Atmos.*, *116*(D2), D02306. https://doi.org/10.1029/2010JD015065

Khosrawi, F., Lossow, S., Stiller, G. P., Rosenlof, K. H., Urban, J., Burrows, J. P., Damadeo, R. P., Eriksson, P., García-Comas, M., … Weigel, K. (2018). The SPARC water vapour assessment II: Comparison of stratospheric and lower mesospheric water vapour time series observed from satellites. *Atmos. Meas. Tech.*, *11*(7), 4435–4463. https://doi.org/10.5194/amt-11-4435-2018

Konopka, P., Tao, M. C., Ploeger, F., Hurst, D. F., Santee, M. L., Wright, J. S., and Riese, M. (2022). Stratospheric moistening after 2000. *Geophys. Res. Lett.*, *49*(8), e2021GL097609. https://doi.org/10.1029/2021GL097609

Li, T., Calvo, N., Yue, J., Dou, X. K., Russell, J. M., Mlynczak, M. G., She, C. Y., and Xue, X. H. (2013). Influence of El Niño–Southern Oscillation in the mesosphere. *Geophys. Res. Lett.*, *40*(12), 3292–3296. https://doi.org/10.1002/grl.50598

Li, T., Calvo, N., Yue, J., Russell, J. M., Smith, A. K., Mlynczak, M. G., Chandran, A., Dou, X. K., and Liu, A. Z. (2016). Southern Hemisphere summer mesopause responses to El Niño–Southern Oscillation. *J. Climate*, *29*(17), 6319–6328. https://doi.org/10.1175/JCLI-D-15-0816.1

Liu, X., Xu, J. Y., Yue, J., Liu, Y. K., and Andrioli, V. F. (2024). Trends in the high-latitude mesosphere temperature and mesopause revealed by SABER. *Atmos. Chem. Phys.*, *24*(17), 10143–10157. https://doi.org/10.5194/acp-24-10143-2024

Lossow, S., Hurst, D. F., Rosenlof, K. H., Stiller, G. P., Von Clarmann, T., Brinkop, S., Dameris, M., Jöckel, P., Kinnison, D. E., … Tao, M. C. (2018). Trend differences in lower stratospheric water vapour between Boulder and the zonal mean and their role in understanding fundamental observational discrepancies. *Atmos. Chem. Phys.*, *18*(11), 8331–8351. https://doi.org/10.5194/acp-18-8331-2018

Nedoluha, G. E., Gomez, R. M., Boyd, I., Neal, H., Allen, D. R., Lambert, A., and Livesey, N. J. (2023). Measurements of stratospheric water vapor at Mauna Loa and the effect of the Hunga Tonga eruption. *J. Geophys. Res.: Atmos.*, *128*(8), e2022JD038100. https://doi.org/10.1029/2022JD038100

Randel, W. J., Wu, F., Vömel, H., Nedoluha, G. E., and Forster, P. (2006). Decreases in stratospheric water vapor after 2001: Links to changes in the tropical tropopause and the Brewer–Dobson circulation. *J. Geophys. Res.: Atmos.*, *111*(D12), D12312. https://doi.org/10.1029/2005JD006744

Remsberg, E., Damadeo, R., Natarajan, M., and Bhatt, P. (2018). Observed responses of mesospheric water vapor to solar cycle and dynamical forcings. *J. Geophys. Res.: Atmos.*, *123*(7), 3830–3843. https://doi.org/10.1002/2017JD028029

Rong, P. P., Russell, J. M., Marshall, B. T., Gordley, L. L., Mlynczak, M. G., and Walker, K. A. (2019). Validation of water vapor measured by SABER on the TIMED satellite. *J. Atmos. Sol. Terr. Phys.*, *194*, 105099. https://doi.org/10.1016/j.jastp.2019.105099

Russell, J. M., III, Mlynczak, M. G., Gordley, L. L., Tansock, J. J., Jr., and Esplin, R. W. (1999). Overview of the SABER experiment and preliminary calibration results. In *Proceedings Volume 3756, Optical Spectroscopic Techniques and Instrumentation for Atmospheric and Space Research III* (pp. 277–288). Denver, CO, USA: SPIE. https://doi.org/10.1117/12.366382

Sheese, P. E., Walker, K. A., Boone, C. D., and Plummer, D. A. (2025). Quantifying the sources of increasing stratospheric water vapour concentrations. *Atmos. Chem. Phys.*, *25*(10), 5199–5213. https://doi.org/10.5194/acp-25-5199-2025

Sheng, Z., He, Y., Wang, S. C., Chang, S. J., Leng, H. Z., Wang, J., Zhang, J., Wang, Y., Zhang, H. W., … Song, J. Q. (2025). Dynamics, chemistry, and modeling studies in the aviation and aerospace transition zone. *Innovation*, *6*(8), 101012. https://doi.org/10.1016/j.xinn.2025.101012

Shi, G. C., Krochin, W., Sauvageat, E., and Stober, G. (2023). Ozone and water vapor variability in the polar middle atmosphere observed with ground-based microwave radiometers. *Atmos. Chem. Phys.*, *23*(16), 9137–9159. https://doi.org/10.5194/acp-23-9137-2023

Smith, A. K. (2012). Global dynamics of the MLT. *Surv. Geophys.*, *33*(6), 1177–1230. https://doi.org/10.1007/s10712-012-9196-9

Tapping, K. F. (2013). The 10.7 cm solar radio flux ($F_{10.7}$). *Space Weather*, *11*(7), 394–406. https://doi.org/10.1002/swe.20064

Yang, C. Y., Li, T., Lai, D. X., Wang, X. Y., Xue, X. H., and Dou, X. (2022). The delayed response of the troposphere-stratosphere-mesosphere coupling to the 2019 southern SSW. *Geophys. Res. Lett.*, *49*(23), e2022GL101759. https://doi.org/10.1029/2022GL101759

Yu, W. D., Garcia, R., Yue, J., Russell, J., and Mlynczak, M. (2022). Variability of water vapor in the tropical middle atmosphere observed from satellites and interpreted using SD-WACCM simulations. *J. Geophys. Res.: Atmos.*, *127*(13), e2022JD036714. https://doi.org/10.1029/2022JD036714

Yu, W. D., Garcia, R., Yue, J., Smith, A., Wang, X. Y., Randel, W., Qiao, Z. S., Zhu, Y. Q., Harvey, V. L., … Mlynczak, M. (2023a). Mesospheric temperature and circulation response to the Hunga Tonga–Hunga Ha'apai volcanic eruption. *J. Geophys. Res.: Atmos.*, *128*(21), e2023JD039636. https://doi.org/10.1029/2023JD039636

Yu, W. D., Yue, J., Garcia, R., Mlynczak, M., and Russell, J. (2023b). WACCM6 projections of polar mesospheric cloud abundance over the 21st century. *J. Geophys. Res.: Atmos.*, *128*(15), e2023JD038985. https://doi.org/10.1029/2023JD038985

Yue, J., Russell, J., III, Gan, Q., Wang, T., Rong, P. P., Garcia, R., and Mlynczak, M. (2019). Increasing water vapor in the stratosphere and mesosphere after 2002. *Geophys. Res. Lett.*, *46*(22), 13452–13460. https://doi.org/10.1029/2019GL084973

Zhang, S. R., Cnossen, I., Laštovička, J., Elias, A. G., Yue, X. N., Jacobi, C., Yue, J., Wang, W. B., Qian, L. Y., and Goncharenko, L. (2023). Long-term geospace climate monitoring. *Front. Astron. Space Sci.*, *10*, 1139230. https://doi.org/10.3389/fspas.2023.1139230

Zhao, Q., and Zhou, X. (2026). Stratospheric transport and residence time of Hunga volcanic aerosol. *Earth Planet. Phys.*, *10*(1), 167–175. https://doi.org/10.26464/epp2026009